NJC

Accepted Manuscript

ROYAL SOCIETY OF CHEMISTRY

rsc.li/njc

View Article Online
DOI: 10.1039/C8NJ03170C

Journal Name

ARTICLE

Melamine Formaldehyde - Metal Organic Gel Interpenetrating Polymer Network Derived Intrinsic Fe-N- Doped Porous Graphitic Carbon Electrocatalysts for Oxygen Reduction Reaction

Received 00th January 20xx,
Accepted 00th January 20xx

DOI: 10.1039/x0xx00000x

www.rsc.org/

Kottarathil Shijina,[a,b] Rajith Illathvalappil,[b,c] Sumitha N. S.,[d] G. S. Sailaja,*[d] Sreekumar Kurungot,[b,c] Balagopal N. Nair,[e,f] A. Peer Mohamed,[a] Gopinathan M. Anilkumar,[e] Takeo Yamaguchi[g] and U. S. Hareesh*[a,b]

Fe, N doped porous graphitic carbon electrocatalyst (Fe-MOG-MF-C), obtained by the pyrolysis of an Interpenetrating Polymer Network (IPN) comprised of melamine formaldehyde (MF as hard segment) and Metal-Organic Gel, (MOG as soft segment) exhibited significant Oxygen Reduction Reaction (ORR) activity in alkaline medium. BET surface area analysis of the Fe-MOG-MF-C evidenced high surface area (821 m^2g^{-1}) while TEM, Raman and XPS results confirmed Fe and N co- doping. Furthermore, a modulated porous morphology with a higher degree of surface area (950 m^2g^{-1}) has been accomplished for the system (Fe-MOG-MFN-C) with the aid of a sublimable porogen like naphthalene. The XPS results further demonstrated that these systems are characterized by a better degree of distribution of graphitic N and exhibited onset potential value of 0.91 V vs RHE in 0.1 M KOH solution following the efficient four-electron ORR pathway. The electrocatalytic activity of Fe-MOG-MFN-C is superior to Fe-MOG-MF-C by virtue of its higher graphitic N content and surface area. The study thus presents a new class of IPN derived MF-MOG nanocomposites with the potential to generate extended versions of *in situ* Fe-N doped porous graphitic carbon structures with superior ORR activity.

Introduction

Fuel cells (FCs) are well accepted as highly efficient, sustainable and green energy resources.[1-3] Anion exchange membrane fuel cells (AEMFCs) are acquiring better acceptance over acidic proton exchange membrane fuel cells (PEMFCs) owing to its several advantages.[4,5] The sluggish kinetics of oxygen reduction reactions (ORR) and the extensive use of expensive platinum (Pt)-based catalyst are the major barriers for the commercialisation of fuel cells.[6-8] The enhanced ORR activity, feasibility of employing Pt free electrocatalysts, choice of liquid fuels such as alcohol and formic acid as an alternative to pure hydrogen together with superior efficiency are the major advantages of AEMFCs.

The quest for high functional, cost-effective catalyst systems alternative to Pt-based systems is primarily focused on the domain of heteroatom doped porous carbon structures.[9-11] Combination of Iron and Nitrogen (Fe, N) doping is widely pursued, as Fe, N coordination on doped nitrogen induce implicit effects on enhancing the electrocatalytic properties due to the added positive charge densities on neighbouring carbon atoms.[12-14] Fe/N/C catalysts with good stability are generally synthesized by high temperature treatment of a variety of precursors.[15-18] Diverse methods such as pyrolysis,[19] chemical vapour deposition,[20] and template method[21] are employed for the synthesis of porous carbons. Among these, pyrolysis of suitable carbon precursors such as MOF and ZIF accomplished significant interest specifically due to the flexibility in design, and improved morphology control.[22,23] However, toxic solvents and tedious procedures are involved in the synthesis of these materials.[10] Hence it is necessary to develop new class of precursor materials with easy synthetic procedures and higher degree of porosity. MOGs are considered to be excellent precursors because of the high surface area with heteroporous nature, design flexibility and less expensive synthetic procedure using less toxic solvents.[24,25] N-doped carbon, for example, obtained by the pyrolytic treatment of Al-MOG doped with N-

[a] Materials Science and Technology Division (MSTD), CSIR-National Institute for Interdisciplinary Science and Technology (CSIR-NIIST) Industrial Estate PO, Thiruvananthapuram, Kerala 695019, India
Email: hareesh@niist.res.in
[b] Academy of Scientific and Innovative Research, Delhi-Mathura Road, New Delhi 110025, India.
[c] Physical and Materials Chemistry Division, CSIR-National Chemical Laboratory, Pune, Maharashtra 411008, India.
[d] Department of Polymer Science and Rubber Technology, Cochin University of Science and Technology, Kochi- 682022, Kerala, India.
Email: sailajags@cusat.ac.in
[e] R&D Centre, Noritake Company LTD, 300 Higashiyama, Miyoshi, Aichi 470-0293, Japan.
[f] Nanochemistry Research Institute, Department of Chemistry, Curtin University, GPO Box U1987, Perth, Western Australia 6845, Australia
[g] Laboratory for Chemistry and Life Science, Institute for Innovative Research, Tokyo Institute of Technology, Nagatsuta 4259, Midori-ku, Yokohama, Kanagawa 226-8503, Japan

†Electronic Supplementary Information (ESI) available: [details of any supplementary information available should be included here]. See DOI: 10.1039/x0xx00000x

View Article Online
DOI: 10.1039/C8NJ03170C

precursor offered electrode materials with high surface area and electron transfer capability.[26]

Inter penetrating polymer networks (IPN) with a minimum of two non-covalently bonded macromolecular networks have been recently envisioned as very good resources for a multitude of applications.[27,28] It is difficult to separate the individual components as the IPN structures are very strong.[29] The reactivity of individual polymers can be modulated to accomplish desired physical and chemical stability.[30] Due to such attributes, IPN systems are employed as gas separation agents,[31] drug delivery systems[32], artificial implants, dialysis membranes, burn dressings etc.[33-37]

Herein, we present the synthesis of Fe-N- doped IPN based porous carbon structures, derived from two individual networks without any covalent bond in between.[38,39] By judicious selection of precursor materials, the resultant network topology could be modulated[40,41] offering feasibility of designing new materials with controllable properties like porosity that primarily originates from its large interspace free volume.[42,43]

The Fe-N *in situ* integrated porous graphene structures presented here are derived from nitrogen abundant thermosetting polymer melamine formaldehyde (MF) and an iron containing MOG. The pre-polymer of MF when intercalated to the primary phase of iron-MOG, propagates simultaneously to generate the hard segment (MF) and soft segment (MOG) of the IPN. The introduction of MF pre-polymer into MOG precursor maximize the addition effect of the resulting polymer network and thereby improves its mechanical properties leading to a stable end product upon pyrolysis.[44] The strong covalently bonded organic polymer MF thus serves as a less expensive nitrogen enriched precursor of carbon. Even though melamine has been explored previously as a nitrogen resource,[45-47] neither of these studies explored the feasibility of MF based IPN systems.

Experimental

Materials

Anhydrous iron (III) chloride ($FeCl_3$), benzene-1,3,5-tricarboxylic acid (H_3BTC or trimesic acid), melamine ($C_3H_6N_6$) and formaldehyde were purchased from Sigma Aldrich Chemical Reagent Co. Ltd. Ethanol (99.9%) was procured from Jiangsu Huaxi International Trade Co-Ltd. China. Potassium hydroxide and tetrahydrofuran (THF) from Merck India and Naphthalene ($C_{10}H_8$) from TCI Chemicals, India Pvt. Ltd. All the reagents were used as received for the synthesis without any further purification.

Synthesis of Fe-MOG-MF and Fe-MOG-MFN IPNs

The Fe-MOG-MF IPN was prepared from Fe-MOG and MF pre-polymer. Fe-MOG (reactant A) was initially prepared by mixing ethanolic solutions of benzene-1,3,5-tricarboxylic acid and anhydrous $FeCl_3$ in the molar ratio of 1:3 at room temperature. Melamine formaldehyde (MF) pre-polymer (reactant B) was synthesized by reacting melamine and formaldehyde in the molar ratio of 1:3 at 70 °C. Upon mixing the reactants A and B, the individual networks are allowed to propagate simultaneously to generate the IPN at room temperature for overnight. In the alternative synthesis of Fe-MOG-MFN, naphthalene, a sublimable porogen (10%, w/w) was introduced to MF pre-polymer matrix as a solution in THF, which was subsequently added to the Fe-MOG. The individual networks of Fe-MOG and MF are allowed to propagate as in the previous case by keeping at room temperature for overnight. The IPNs formed were dried at 50 °C for overnight followed by cross-linking of MF at 120 °C in an air oven for 48 h.

Synthesis of Fe-N doped porous carbon

Fe-N-doped graphitic carbons from Fe-MOG-MF and Fe-MOG-MFN IPNs were derived by pyrolysis of the corresponding precursors at 900 °C for 3h under N_2 atmosphere. Any unbound Fe present in the pyrolyzed samples were washed out with 3 M H_2SO_4 solution followed by rinsing with DI water for several times and dried at 50 °C. The samples derived were denoted as Fe-MOG-MF-C and Fe-MOG-MFN-C.

Structural Characterization

X-ray diffraction patterns were collected with PW1710 Philips, The Netherlands (Cu Kα 1.54 Å). The BET surface area and porosity analysis of the samples were performed with Micromeritics (Tristar 11, USA) surface area analyser using nitrogen adsorption at 77 K. The samples were degassed at 200 °C for 2 h in flowing N_2 before adsorption measurements. Raman spectra were obtained from a Confocal Raman microscope (alpha 300 R WITEC Germany) using 633 nm laser. The microstructure and morphology of the samples were observed with scanning electron microscope (SEM Carl Zeiss, Germany) and elemental mapping was carried out using energy dispersive spectroscopy (EDS). Transmission electron micrographs of samples were recorded on a FEI (Tecnai 30 G2 S-TWIN, The Netherlands) microscope. The Rheological properties of the samples were measured using a Modular Compact Rheometer (MCR102, Anton Paar, India). XPS was investigated using a scanning X-ray microprobe (ULAC-PHI, Inc. PHI-4700 V, USA) with monochromated Al-Kα X-ray source operating at 14 kV and 220 W.

Electrochemical Characterization

ORR measurements were carried out in a Bio-Logic Electrochemical Workstation (SP-300) using a three-electrode setup. The catalyst ink for ORR study was prepared by mixing 5 mg of the catalyst with 1 mL of DI water-isopropyl alcohol mixture (3:1) and 40 µL of 5 wt. % nafion for 60 min in an ultrasonic bath. 10 µL of this catalyst slurry was drop casted on the surface of a glassy carbon working electrode (0.196 cm^2) using a micro syringe. The electrode was dried under an IR lamp for electrochemical analysis. Commercial Pt/C (40 wt. % from Johnson Mattey) was also studied for the comparison purpose. 0.1 M KOH was used as the electrolyte for the electrochemical

measurements. Catalyst coated glassy carbon disc (0.196 cm^2 area, Pine Instruments. Inc.) was used as the working electrode. Hg/HgO was used as the reference electrode and graphite rod was used as the counter electrode. Cyclic voltammetry (CV) was performed at a scan rate of 50 mV s^{-1} in both nitrogen and oxygen saturated 0.1 M KOH solution. Linear sweep voltammetry (LSV) was carried out by recording the voltammograms at a scan rate of 5 mV s^{-1}. The accelerated durability analysis of both Fe-MOG-MFN-C and Pt/C was carried out by running CV for 5000 cycles in a potential window of 0.97 to 0.57 V. All these measurements were carried out using a Rotating Disk Electrode (RDE, 0.196 cm^2, Pine Instruments). Hydrogen peroxide percentage and number of electrons transferred during the oxygen reduction reaction were measured using a rotating ring disc electrode (RRDE, 0.2826 cm^2, Pine Instruments) in O_2 saturated 0.1 M KOH solution with a glassy carbon disc (0.2826 cm^2) having a platinum ring as the working electrode, Hg/HgO as the reference electrode and graphite rod as the counter electrode. All potentials were converted into RHE by calibrating Hg/HgO in H_2 saturated 0.1 M KOH solution[48] (Figure S1).

Results and Discussion

We report a simple and highly feasible method for the Fe-N-intrinsic doping via formation of IPN from an organic thermosetting polymer enriched with N and a metal (Fe)-organic gel network. The competing growth of the propagating organic and inorganic chains lead to a stable network with soft and hard segments (Fe-MOG-MF), which upon pyrolysis undergo restructuring to generate highly porous graphitic sheets with firmly anchored Fe and N. The introduction of naphthalene in the MF polymer (Fe-MOG-MFN) has been examined as a strategy to enhance surface area of Fe-MOG-MFN. Upon pyrolysis, this material resulted in the formation of porous carbon with enhanced surface area due to the sublimation of the dissolved naphthalene. Figure 1 illustrates the schematic illustration of formation of Fe-MOG-MFN-C.

The formation of Fe-MOG is characterized by rheological analysis. It was done using amplitude sweep test, where the strain percentage was kept between 0.01 to 10%. The storage modulus (G') and loss modulus (G") were measured at a constant temperature of 25 °C and 10 rad/s frequency. Figure 2 shows the range of viscoelastic properties of the gel as a function of strain. Fe-MOG exhibited values of G' higher than G" upto a particular strain value. This means the elasticity of the gel is higher than the viscous behaviour, producing a well viscoelastic and stable gel. When G' and G" approaches the crossover point, breaking down of gel network results. The cross over strain value for Fe-MOG is 5.95% indicating better stability of the formed gel network.

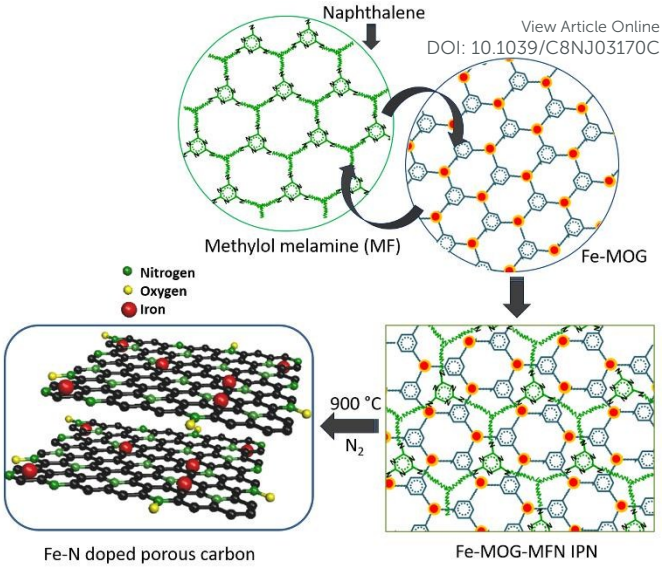

Figure 1. Schematic illustration for the formation of Fe-MOG-MFN-C.

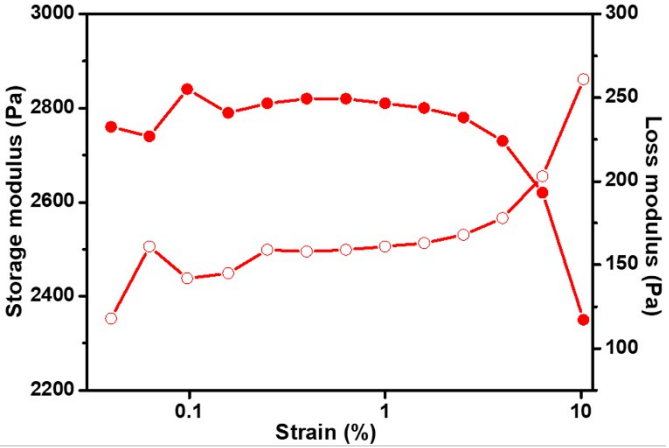

Figure 2. Amplitude sweep measurement of Fe-MOG. Solid and open symbol represent the storage and loss modulus respectively.

The SEM images of Fe-MOG-MF-C and Fe-MOG-MFN-C (Figure 3) indicate morphological diversity as a function of naphthalene content in the system. The sheet-like graphitized carbon structures are connected by elongated and better distributed pores in Fe-MOG-MFN-C (Figure 3c, d). For Fe-MOG-MF-C, only fewer pores are visible even though the macro-pores are evenly distributed, (Figure 3a, b) demonstrating that naphthalene indigenously plays vital role in modulating the macro-porous structure and morphology of the system.

The presence of C, N, O and Fe can be clearly visualized in the elemental mapping shown in figures 3e and f. The homogeneous distribution of N and Fe in the carbon framework is clearly seen from the corresponding elemental maps.

View Article Online
DOI: 10.1039/C8NJ03170C

Journal Name

ARTICLE

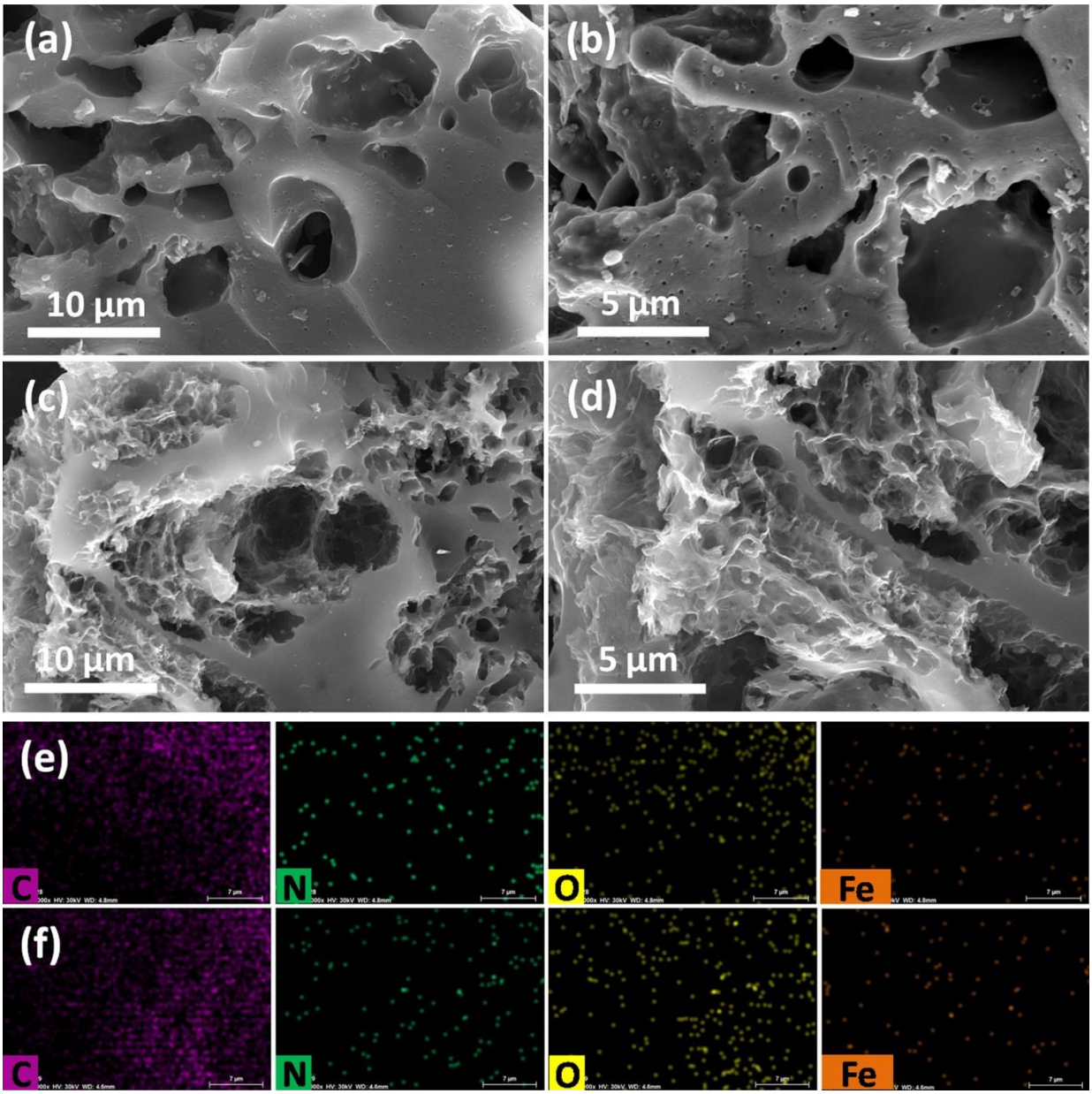

Figure 3. SEM images of (a, b) Fe-MOG-MF-C and (c, d) Fe-MOG-MFN-C, Elemental mapping of (e) Fe-MOG-MF-C and (f) Fe-MOG-MFN-C.

The HRTEM images of Fe-MOG-MF-C and Fe-MOG-MFN-C (Figure 4) confirm sheet-like graphitized carbon structures. Fe-MOG-MF-C and Fe-MOG-MFN-C exhibit morphological diversity. Low magnification images of Fe-MOG-MF-C appear as thin layered structures which are composed of interconnected entangled chains (Figure 4a). The lattice spacing of 0.34 nm is consistent with (002) plane of graphitic carbon (Figure 4b).[49-51] Nanoparticles with darker contrast are clearly identified. The higher magnification image of the nanoparticle in figure 4c displays crystallized structure with the lattice spacing of 0.205 nm corresponding to the (220) plane of Fe_3C.[52,53] Fe-MOG-MFN-C exhibits two phase morphology coherent to each other and consisted of star-like structures distributed well-over graphitic sheets of approximately 20 nm thick with regular lattice arrangement at several regions (Figure 4d, e). This remarkable difference in the nano geometry is noticed upon the

View Article Online
DOI: 10.1039/C8NJ03170C

Journal Name

ARTICLE

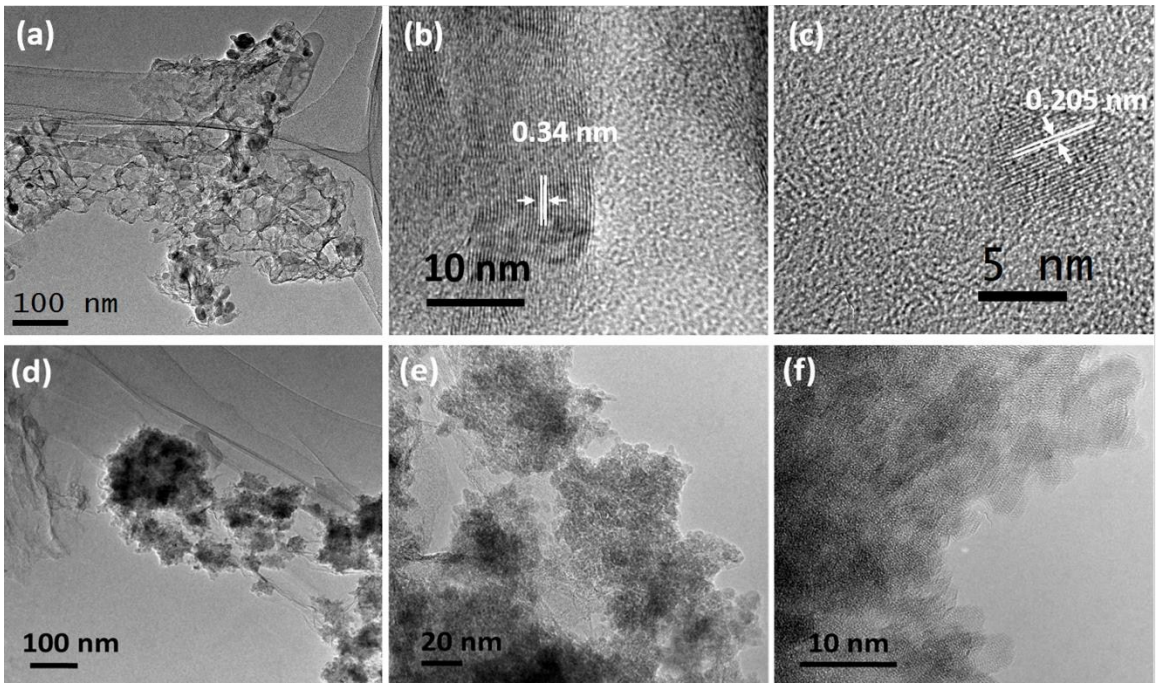

Figure 4. TEM images of (a, b, c) Fe-MOG-MF-C and (d, e, f) Fe-MOG-MFN-C.

incorporation of naphthalene, and is apparent from the mixed structure of Fe-MOG-MFN-C given in figure 4d-f. The well-defined interconnected network type organization shown by both Fe-MOG-MF-C and Fe-MOG-MFN-C at higher magnification demonstrates the structural features of the initial template that confirms the generation of the proposed inter-penetrating network system, from which the carbon matrices are derived. It should also be noted here that; more diverse structure and a higher surface area is possessed by the graphitic sheets synthesized here as compared to the nano graphene sheets prepared by Peng *et al* from the pyrolytic treatment of melamine and an iron precursor.[12]

The surface characteristics of carbon products are quantified from N_2 adsorption-desorption analysis (performed at 77 K). The carbon materials exhibited high surface area values of 821 m^2g^{-1} and 950 m^2g^{-1} respectively for Fe-MOG-MF-C and Fe-MOG-MFN-C. The pore structure was predominantly microporous (Figure 5a). The type II b isotherms having adsorption hysteresis indicated the presence of mesopores along with these micropores. The increased mesoporosity in Fe-MOG-MF-C sample can be clearly visible from the inset graph in figure 4a. For Fe-MOG-MFN-C sample, increased microporosity is observed due to the sublimation of naphthalene. The cumulative pore volume measured from BJH was found to be 0.10 $cm^3\ g^{-1}$and 0.07 $cm^3\ g^{-1}$ respectively for Fe-MOG-MF-C and Fe-MOG-MFN-C respectively (Figure 5b). The mesopore size distribution curve obtained from BJH method, shown in figure 5c, has a pore size distribution within 2-12 nm for both the samples. Fe-MOG-MF-C sample seems to have slightly better pore size distribution. The micropore size distribution curves obtained from NLDFT analysis show the variation of micropore volume for the two samples (Figure 5d). Both the samples showed a narrow pore size distribution within 0.5-2.0 nm with a slightly higher micropore volume for Fe-MOG-MFN-C sample.

View Article Online
DOI: 10.1039/C8NJ03170C

Journal Name

ARTICLE

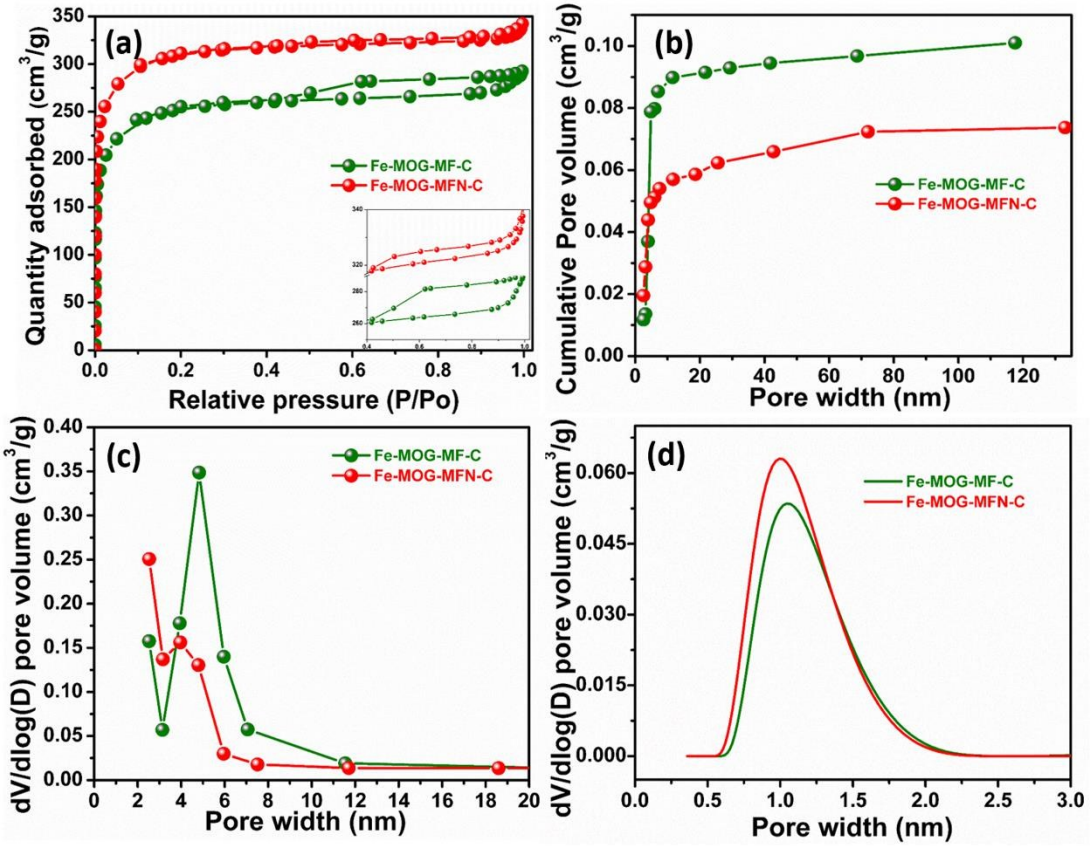

Figure 5. (a)N_2 adsorption-desorption isotherms of Fe-MOG-MF-C and Fe-MOG-MFN-C, (b) BJH cumulative pore volume and (c) pore size distribution of Fe-MOG-MF-C and Fe-MOG-MFN-C (d) NLDFT pore size distribution of Fe-MOG-MF-C and Fe-MOG-MFN-C.

Both Fe-MOG-MF-C and Fe-MOG-MFN-C consist of amorphous graphitized carbon, as confirmed from the XRD patterns (Figure 6). Reflection peaks corresponding to 2θ values of 26° and 44° are indexed to (200) and (101) lattice of graphitic carbon respectively (JCPDS: 75-1621).[54,55] It could be envisaged that for Fe-MOG-MFN-C, the broader peak (002) indicates increased degree of amorphous nature/ disorder in the structure[56] derived due to the presence of naphthalene in the system which is further corroborated by Raman spectrum. No peak corresponding to Fe_3C was visible. This is presumed to be due to the disordered incorporation of iron atom in the carbon matrix and also due to its lower percentage in the carbon structure. The purity of Fe-MOG-MF-C and Fe-MOG-MFN-C are substantiated by the absence of any impurity peaks.

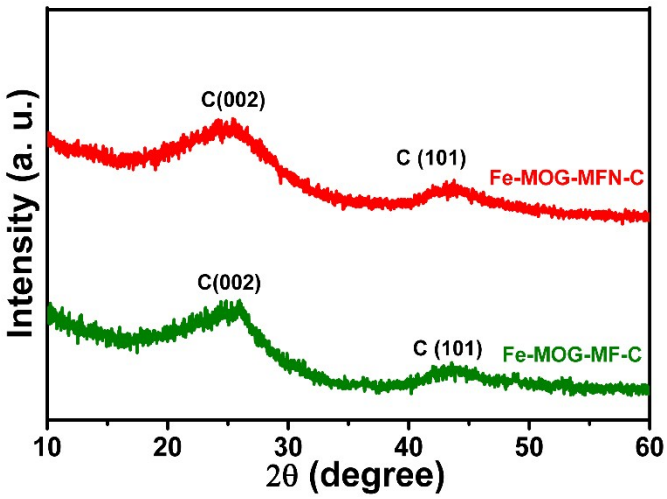

Figure 6. Powder X-ray diffraction patterns of Fe-MOG-MF-C and Fe-MOG-MFN-C.

Raman spectral interpretation is a standard tool endowed with important structural information of the graphitic, distorted, crystalline or amorphous carbon materials.[57] For Fe-MOG-MF-C (Figure 7), the G band arising from the bond stretching of sp^2 hybridized carbon atoms of the hexagonal graphitic rings is observed at 1594 cm^{-1} while D band resulting from the distorted carbon frames on the defect sites was at 1344 cm^{-1}.[58-60] For Fe-MOG-MFN-C Raman spectra indicated peak at 1604 cm^{-1} corresponding to G band and 1352 cm^{-1} representing D band. The proportionality term I_D/I_G imparts insights on the degree of distortion of the carbon structure, as the distortion increases with increasing I_D/I_G ratio. Fe-MOG-MF-C has I_D/I_G ratio of 0.78, indicating higher degree of graphitization, whereas Fe-MOG-MFN-C displayed I_D/I_G ratio of 1.23 suggesting a greater disorder indicating increased nitrogen content. The increased disorder should be attributed to the structural changes occurring during the sublimation of naphthalene. In order to elucidate the influence of pyrolysis temperature on the nitrogen content and degree of graphitization, the precursor Fe-MOG-MFN was carbonized at 800 and 1000 °C for 3 h at a heating rate of 3 °C/min in N_2 atmosphere. The obtained Raman spectra for 800 and 1000 °C pyrolyzed samples are shown in Figure S2. The I_D/I_G ratio is found to be 1.12 and 0.93 respectively for Fe-MOG-MFN-C-800 and Fe-MOG-MFN-C-1000. The ratio initially increases with temperature and after 900 °C, decreases. This is due to the removal of nitrogen at temperatures greater than 900 °C. Fe-MOG-MFN-C (pyrolyzed at 900 °C) is assumed to perform greater catalytic activity because of the increased graphitic N content. The influence of pyrolysis temperature on the ORR activity with will be discussed later in the paper.

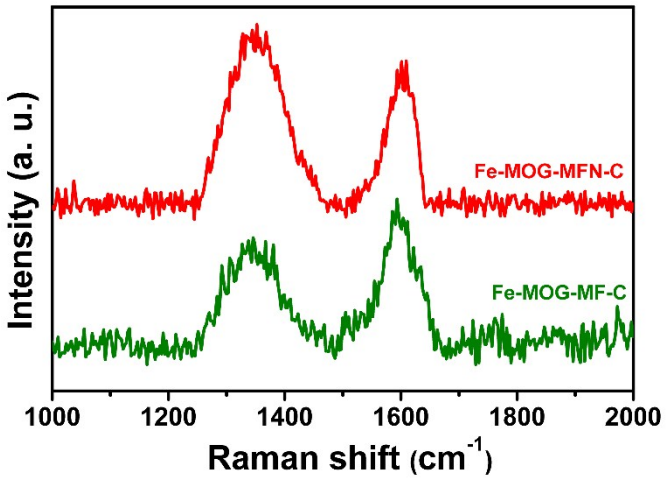

Figure 7. Raman spectra of Fe-MOG-MF-C and Fe-MOG-MFN-C.

The X-ray Photoelectron spectra (XPS) confirmed elemental composition of Fe-MOG-MF-C and Fe-MOG-MFN-C as C, Fe, N, O and their chemical states (Figure 8). From the regional scan of N 1s spectrum (Figure 9a), three major N species as pyridinic N (N1, 398.51 eV), graphitic N (N2, 400.90 eV) and oxidized N (N3, 403.70 eV) are noticed. No peak corresponding to pyrrolic N is observed which is probably owing to its very low concentration. The oxidised N is presumably formed as a result of the adsorption of oxygen in air at the N-doped sites.[61,62] In Fe-MOG-MF-C, graphitic N is the higher fraction (1.91 at.%) and pyridinic N comes next (0.82 at.%). Since there is only a small difference between the binding energies of N-Fe bond and pyridinic N, the peak at 398.5 eV represent the form of nitrogen bonded to metal also.[63-65] The higher fractions of graphitic and pyridinic N content influence the improved electrocatalytic activity of the carbon as the presence of appreciable amount of pyridinic and graphitic N is responsible for the catalytic performance.[66,67]

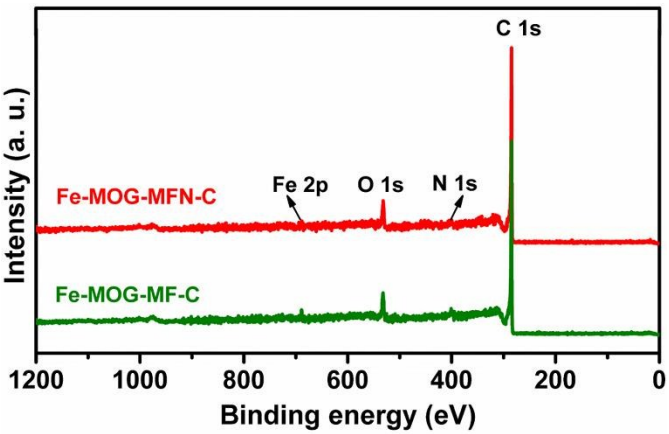

Figure 8. XPS survey scan spectrum of Fe-MOG-MF-C and Fe-MOG-MFN-C.

The deconvoluted N 1s spectrum of Fe-MOG-MFN-C (Figure 9b) also shows the presence of pyridinic (N1, 398.50 eV), graphitic (N2, 401.11 eV) and oxidized N (N3, 404.71 eV). The percentage of different nitrogen species is different for the two samples. Fe-MOG-MFN-C having higher graphitic nitrogen percentage (1.97 at.%) is expected to show good ORR activity.[66] However, the doped Fe content is almost similar in both the samples (0.15 at.%). The concentrations of different nitrogen species for the two samples are evaluated based on the integrated peak areas and the corresponding graph as shown in figure 10.

The nature of doped Fe was confirmed from Fe 2p XPS spectra (Figure 9c, d). The binding energies of Fe $2p_{3/2}$ and Fe $2p_{1/2}$ of Fe^{3+} ion are located at 711.5 and 724.7 eV respectively. The peak at 717.3 eV corresponds to Fe $2p_{3/2}$ satellite peak which is also an indication of the existence of iron oxide phase in the carbon structure.[68-70]

The variation of N and Fe content with pyrolysis temperature was also studied with XPS analysis. The survey spectrum shown in figure S3 confirms the presence of elements C, N, O and Fe. The deconvoluted spectrum of Fe-MOG-MFN-C-800 shows a nitrogen content of 2 at.% and that of Fe-MOG-MFN-C-1000 is 0.5 at.% (Figure S4). This data is in accordance with Raman results. The amount of graphitic N is 1.14 at.% for Fe-MOG-MFN-C-800 and no graphitic nitrogen is detected for Fe-MOG-MFN-C-1000. The variation of concentration of different nitrogen species with pyrolysis temperature is shown in table S1.

View Article Online
DOI: 10.1039/C8NJ03170C

Journal Name

ARTICLE

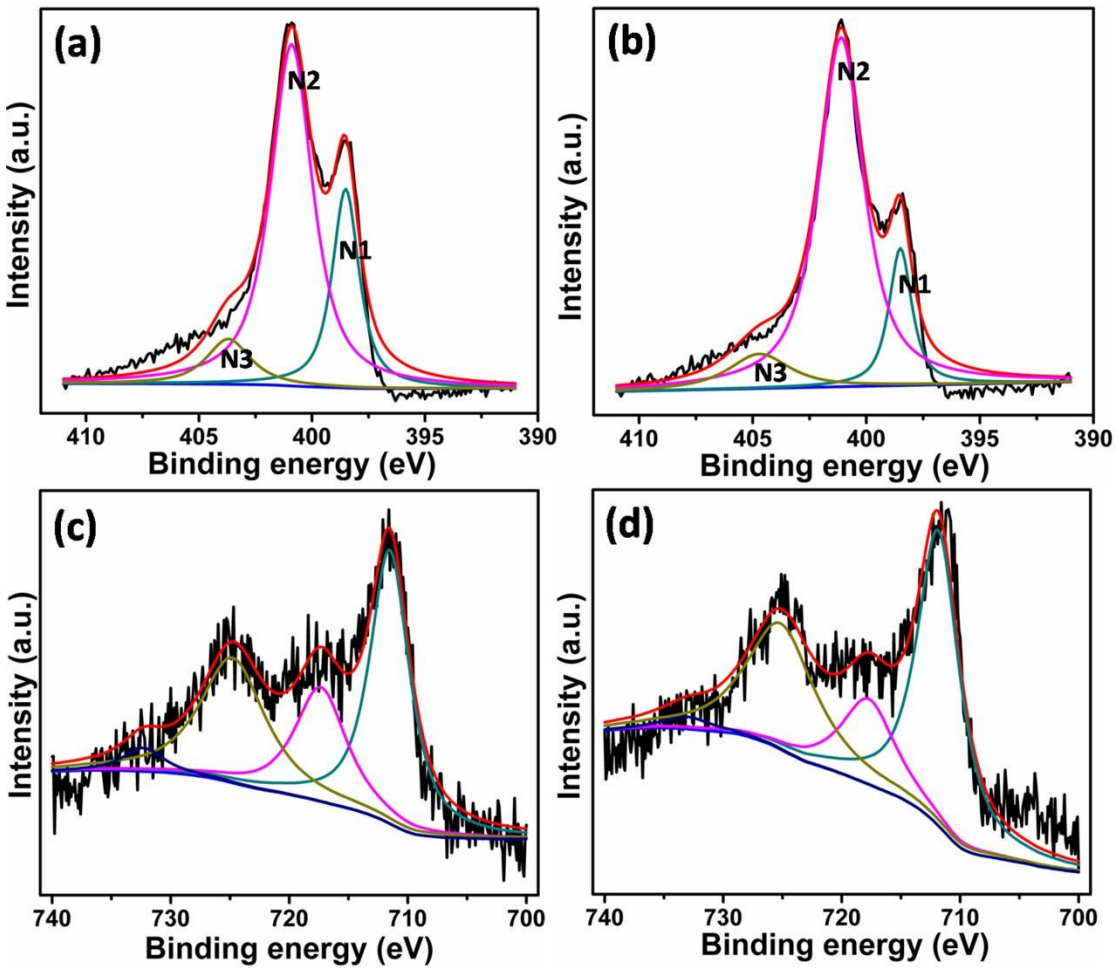

Figure 9. High resolution N 1s XPS spectra of (a) Fe-MOG-MF-C (b) Fe-MOG-MFN-C, High resolution Fe 2p XPS spectra of (c) Fe-MOG-MF-C (d) Fe-MOG-MFN-C.

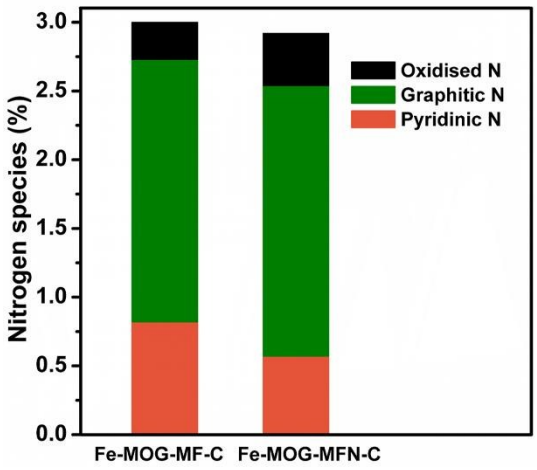

Figure 10. Concentration of various types of Nitrogen (in atomic percentage) present in the Fe- doped carbon catalyst samples.

Cyclic voltammetry (CV) and linear sweep voltammetry (LSV) experiments were performed to measure the electrocatalytic activity of the samples. These RDE experiments were carried out in oxygen saturated 0.1 M KOH with Hg/HgO as the reference electrode, glassy carbon electrode coated with sample as the working electrode and graphite rod as the counter electrode. In order to better understand the role of nitrogen, a control sample was prepared by the same synthetic route without adding nitrogen source (Fe-MOG-C). The SEM image of the control sample displays a porous morphology (Figure S5). Further, TEM image shows sheet like carbon structure in which iron nanoparticles are distributed (Figure S6). The morphology and XRD pattern of control sample (Figure S7) are similar to Fe-MOG-MF-C, whereas the surface area of 352 cm^2/g, (Figure S8) is very less compared to Fe-MOG-MF-C and Fe-MOG-MFN-C samples.

View Article Online
DOI: 10.1039/C8NJ03178C

The comparison of LSVs of Fe-MOG-C, Fe-MOG-MF-C and Fe-MOG-MFN-C in oxygen saturated 0.1 M KOH solution with a rotation rate of 1600 rpm is shown in figure 11a. Both Fe-MOG-MF-C and Fe-MOG-MFN-C samples exhibit an onset potential of 0.91 V and that of Pt/C is 1 V. Even though the onset potentials of Fe-MOG-MF-C and Fe-MOG-MFN-C samples are the same, the limiting current value is higher for Fe-MOG-MFN-C, which is attributed to the increased surface area and graphitic nitrogen content. The onset potential for the control sample is 0.81 V, which is much lower than the above N-doped samples, which corroborates the role of nitrogen species in enhancing the ORR catalytic activity. The effect of pyrolysis temperature on the ORR activity was analyzed by plotting LSVs of samples pyrolyzed at temperatures of 800, 900 and 1000 °C (Figure S9). The onset potential of Fe-MOG-MFN-C 800 and Fe-MOG-MFN-C-900 are 0.91 V, but the limiting current density is higher for 900 °C pyrolyzed sample (-4.5 mA cm^{-2}), which is due to the increased graphitic N content. For 1000 °C pyrolyzed sample, the lower nitrogen content resulted in low the onset potential (0.85 V) and limiting current density (-3.8 mA cm^{-2}).

Figure 11b shows the cyclic voltammograms of Fe-MOG-MFN-C in oxygen and nitrogen saturated 0.1 M KOH solution and the current–voltage profiles are measured at a typical scan rate of 50 mV s^{-1} with a rotation rate of 900 rpm in a potential window of 0.07 to 1.07 V vs. RHE. There is no well-defined peak in N_2 saturated electrolyte. On oxygen purging, the cathodic current increases dramatically indicating the presence of more oxygen reduction sites on Fe-MOG-MFN-C. The CVs of Fe-MOG-MFN-C-800 and Fe-MOG-MFN-C-1000 are also provided (Figure S10). The LSVs of Fe-MOG-MFN-C at different working electrode rotations are also studied and the result showed increased limiting current value with increased electrode rotation because of the enhanced diffusion of electrolyte and mass transfer (Figure 11c). The LSVs for Fe-MOG-MFN-C-800, Fe-MOG-MFN-C-1000, Fe-MOG-MF-C and Pt/C at different working electrode rotations are also presented (Figure S11).

The kinetic parameters of the ORR can be analysed on the basis of the Koutecky–Levich (K–L) equation. K–L slops obtained by plotting inverse of current density (1/j) against inverse of square root of angular density ($1/\omega^{1/2}$). K-L plot of different samples are shown in figure 11d. Good linearity obtained for all the samples. A linear relationship between current density and square root of the rotation speed is obtained for all the samples. The obtained slope is constant at different potentials suggesting similar electron transfer number over this potential range.

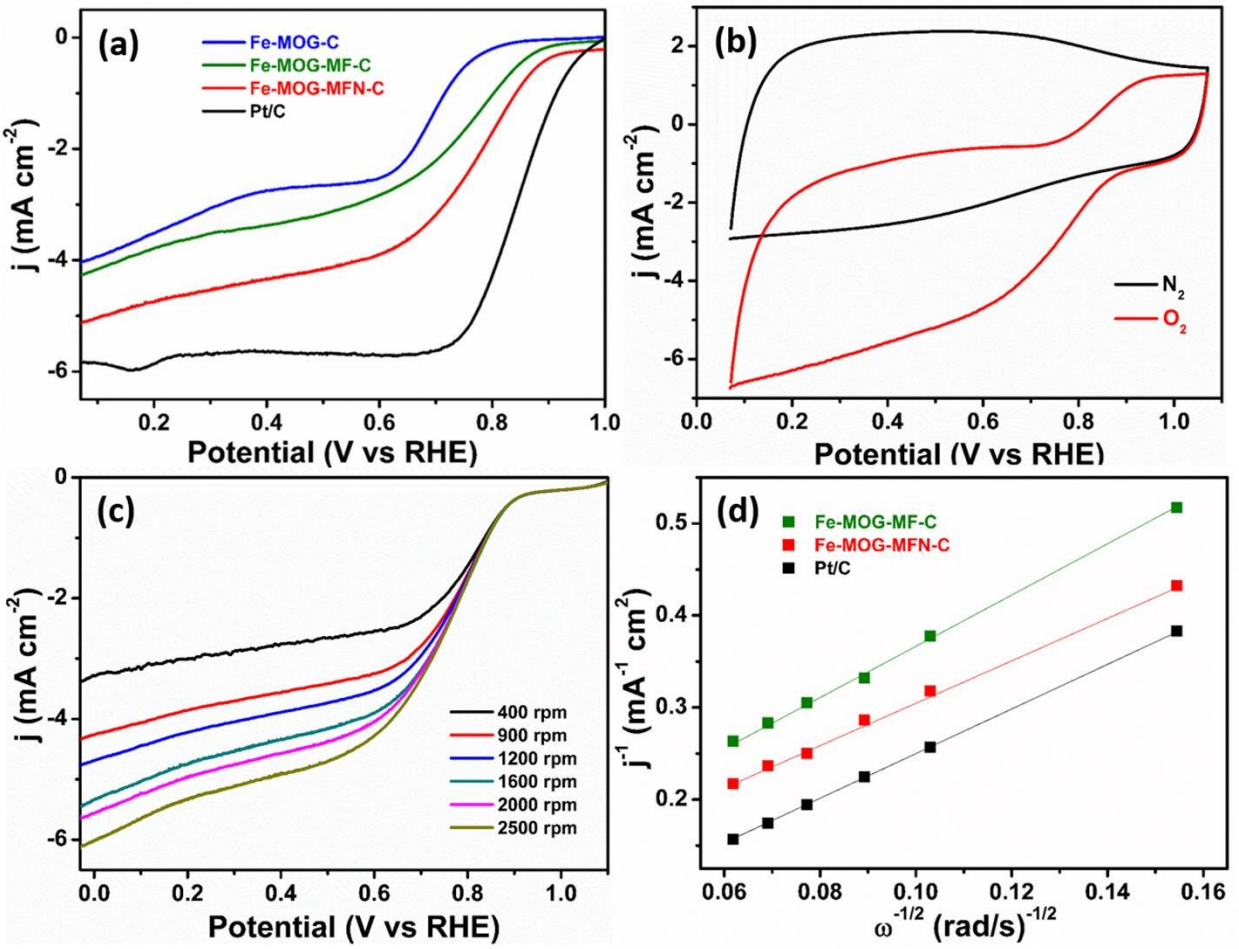

Figure 11. (a) Linear Sweep voltammogram (LSV) comparison in O_2 saturated 0.1 M KOH solution measured at a scan rate of 5 mV sec^{-1} at 1600 rpm, (b) Cyclic voltammograms of Fe-MOG-MFN-C in 0.1 M KOH solution measured at a scan rate of 50 mV sec^{-1} at 900 rpm, (c) LSVs of Fe-MOG-MFN-C in O_2 saturated 0.1 M KOH solution measured at different rotation rates at a scan rate of 5 mV sec^{-1} (d) Comparison of Koutecky-Levich (K-L) plots.

View Article Online
DOI: 10.1039/C8NJ03170C

ARTICLE

RRDE measurements were carried out to investigate the amount of peroxide generated during ORR. Following equations have been used to calculate the percentage of H_2O_2 produced and the number of electron transferred during ORR.

$$H_2O_2(\%) = 200 \times \frac{\frac{I_r}{N}}{I_d + \frac{I_r}{N}} \quad \text{..... (i)}$$

$$n = 4 \times \frac{I_d}{I_d + \frac{I_r}{N}} \quad \text{..... (ii)}$$

where 'I_r' and 'I_d' are the Faradaic ring and disc current, respectively. 'N' is the collection efficiency of the ring electrode (0.37) and the 'n' is the number of the transferred electron.

The amount of H_2O_2 has been quantified by analysing the ring current of the RRDE result. If the amount of peroxide produced is less, the ring current becomes lower since less amount of peroxide reaches the Pt ring electrode. A comparison of percentage of peroxide produced over different catalysts is presented in figure 12a. The peroxide yield on Fe-MOG-MFN-C is estimated to be 20 % which is significantly lower than that of Fe-MOG-MF-C. The Pt/C sample is calculated to produce 5 % H_2O_2. The electron transfer number calculated from H_2O_2 percentage for all the samples are presented in figure 12b. It could be confirmed that Fe-MOG-MFN-C shows an electron transfer number of 3.6 which proves that the preferred ORR kinetics involve a major contribution from the direct reduction of oxygen into water in the system. The increased electron transfer number for Fe-MOG-MFN-C compared to Fe-MOG-MF-C is attributed to the increased surface area and graphitic N content. Tafel slope for Fe-MOG-MFN-C is 83.4 mV/dec and is comparatively lower than Fe-MOG-MF-C indicating faster ORR kinetics (Figure 12c).

In addition to the improved ORR activity, it is important to check the stability of the catalyst under the electrochemical environment. Hence accelerated durability test (ADT) was carried out to compare the stability of the catalyst with respect to Pt/C. The ADT is performed at room temperature in oxygen-saturated 0.1 M KOH at a scan rate of 100 mV s^{-1} for 5000 cycles. Initially, the LSV of Fe-MOG-MFN-C is taken at 1600 rpm to envisage its original ORR performance. After 5000 cycles, LSV is repeated again and degradation in activity was quantified by comparing the half wave potential of the catalyst before and after the ADT test (Figure 12d). The potential drop after 5000 cycles is 31 mV which is lower compared to that of Pt/C, which has a shift of 34 mV (Figure S12).

View Article Online
DOI: 10.1039/C8NJ03170C

Journal Name

ARTICLE

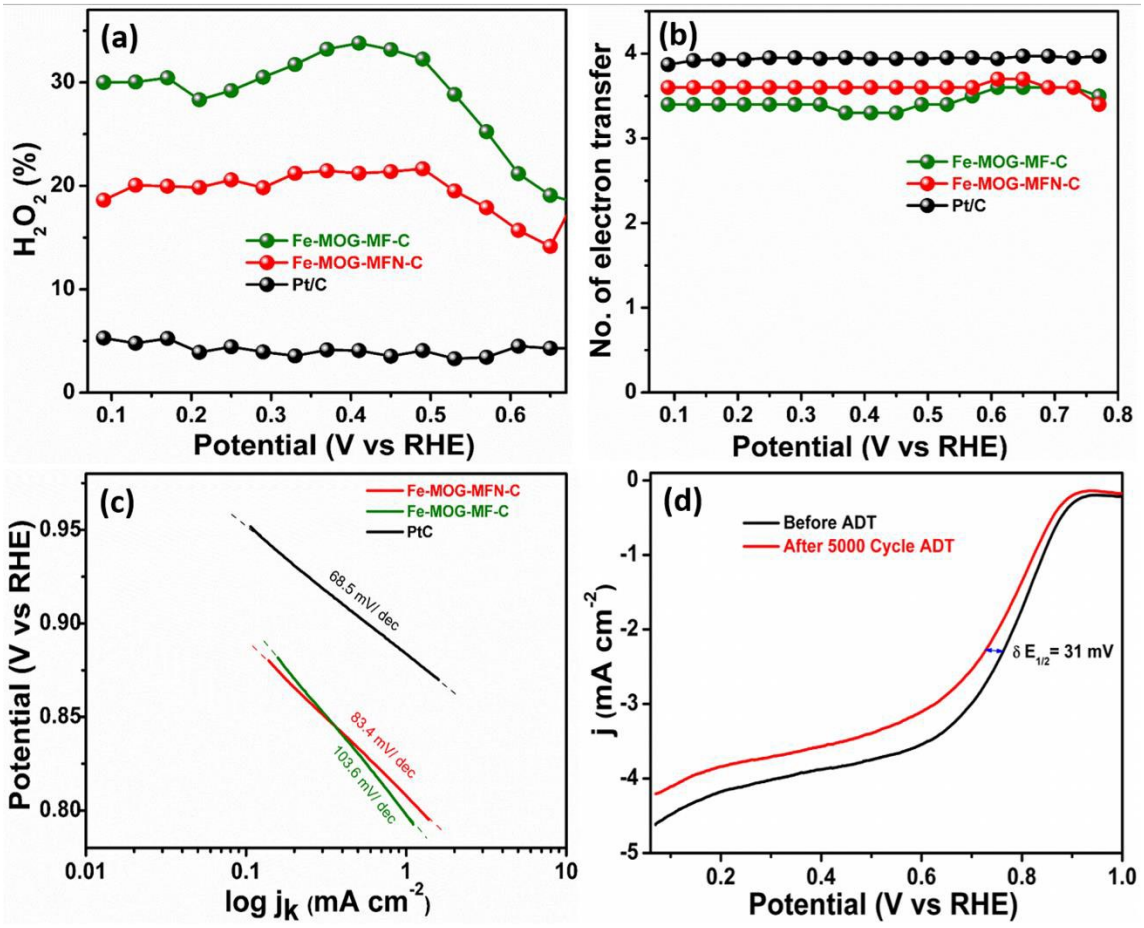

Figure 12. (a) Hydrogen peroxide yield and (b) number of electron transfer comparison at different potentials obtained from the RRDE experiment, (c) Tafel slope comparison of Fe-MOG-MF-C, Fe-MOG-MFN-C with Pt/C, (d) LSV recorded before and after 5000 cycles ADT analysis for Fe-MOG-MFN-C in O_2 saturated 0.1 M KOH solution with electrode rotation of 1600 rpm.

It is implicit that, the design of carbon catalysts with optimum combination of higher surface area, pore structure, amount of doped heteroatoms, pore and dopants distribution and degree of graphitization contribute positively in accomplishing better electrocatalytic activity. It is therefore difficult to specify a single parameter as the governing factor for improved ORR performance of carbon electrocatalysts. The catalysts proposed here were synthesized as high purity hetero-atom (Fe and N) decorated carbon with high surface area, in an economically beneficial route based on a gel-polymer IPN system by using less-expensive melamine formaldehyde as the nitrogen source. Here, we have adopted the technique of intrinsic doping and *in situ* synthesis for realising carbon with both Fe and N as intrinsic part of their composition. The addition of porogen (naphthalene) has influenced the structure characteristics such as morphology and surface area, as seen from the XRD, TEM, BET analysis and ORR performance. The increased microporosity accounts for the pore generation associated with naphthalene sublimation. Fe-MOG-MFN-C contains higher amount of doped graphitic N (1.97) with higher I_D/I_G ratio in the Raman spectrum. It has helped in improving the ORR catalytic activity in Fe-MOG-MFN-C. ORR onset potential was same in both the samples (0.91 V) while the limiting current is higher in Fe-MOG-MFN-C due to the higher surface area. Besides all these properties, a good durability of 5000 cycles also make Fe-MOG-MFN-C a good ORR catalyst.

Conclusions

We have presented a simple synthetic procedure for the preparation of Fe-N intrinsically doped porous graphitic carbon electrocatalysts from Inter penetrating network (IPN) of *in situ* polymerized melamine formaldehyde (hard segment) and metal-organic gel (soft segment). Raman spectroscopic analysis and XPS analysis revealed the successful doping of nitrogen and iron in the graphitic carbon network. The deconvoluted N 1s spectra clearly showed the presence of more amount of nitrogen in the form of graphitic nitrogen as the active site for enhanced ORR activity. No detectable amount of pyrrolic nitrogen was observed. Moreover, high surface area of 950 m^2 g^{-1} also contributed towards the improved ORR activity. The results further demonstrated the feasibility to derive extended versions of *in situ* Fe-N doped porous carbon structures with better ORR activity from IPN based structures via systemic modulations of synthetic protocols and inclusion of porogens.

Conflicts of interest

There are no conflicts to declare.

Acknowledgements

The authors acknowledge Noritake Co. Limited, Aichi, Japan, & the Council of Scientific and Industrial Research (CSIR), New Delhi, India, for providing research facilities and financial support.

Notes and references

.

1 A. Kirubakaran, S. Jain and R. K. Nema, *Renew. Sust. Energ. Rev*., 2009, **13**, 2430-2440.
2 A. Stambouli, Fuel cells: The expectations for an environmental-friendly and sustainable source of energy, 2011.
3 M. Thomas, R. Illathvalappil, S. Kurungot, B. N. Nair, A. Peer Mohamed, G. M. Anilkumar, T. Yamaguchi and U. S. Hareesh, Chemistry Select*,* 2018, **3**, 8688-8697.
4 D. R. Dekel, J. Pow*er Sources*, 2018, **375**, 158-169.
5 T. J. Omasta, A. M. Park, J. M. LaManna, Y. Zang, X. Peng, L. Wang, D. L. Jacobson, J. R. Varcoe, D. S. Hussey, B. S. Pivovar and W. E. Mustain, *Energy Environ. Sci*., 2018, **11**, 551.
6 J. Y. Choi, R. S. Hsu and Z. Chen, *J. Phys. Chem. C*, 2010, **114**, 8048-8053.
7 M. Oezaslan, F. Hasché and P. Strasser, *J. Phys. Chem. Lett.*, 2013, **4**, 3273-3291.
8 J. K. Nørskov, J. Rossmeisl, A. Logadottir, L. Lindqvist, J. R. Kitchin, T. Bligaard and H. Jónsson, *J. Phys. Chem. B*, 2004, **108**, 17886-17892.
9 H. W. Liang, W. Wei, Z.-S. Wu, X. Feng and K. Müllen, *J. Am. Chem. Soc.*, 2013, **135**, 16002-16005.
10 W. Xia, B. Qiu, D. Xia and R. Zou, *Sci. Rep.*, 2013, **3**, 1935.
11 A. S. Jalilov, G. Ruan, C. C. Hwang, D. E. Schipper, J. J. Tour, Y. Li, H. Fei, E. L. G. Samuel and J. M. Tour, *ACS Appl. Mater. Interfaces*, 2015, **7**, 1376-1382.
12 H. Peng, Z. Mo, S. Liao, H. Liang, L. Yang, F. Luo, H. Song, Y. Zhong and B. Zhang, *Sci. Rep.*, 2013, **3**, 1765.
13 J. Liang, R. F. Zhou, X. M. Chen, Y. H. Tang and S. Z. Qiao, *Adv. Mater.*, 2014, **26**, 6074-6079.
14 C. He, T. Zhang, F. Sun, C. Li and Y. Lin, *Electrochim. Acta*, 2017, **231**, 549-556.
15 J. C. Li, S. Y. Zhao, P. X. Hou, R.P. Fang, C. Liu, J. Liang, J. Luan, X. Y. Shan and H.-M. Cheng, *Nanoscale*, 2015, **7**, 19201-19206.
16 S. M. Unni, G. M. Anilkumar, M. Matsumoto, T. Tamaki, H. Imai and T. Yamaguchi, *Sustainable Energy Fuels*, 2017, **1,**1524-1532.
17 F. L. Meng, Z. L. Wang, H. X. Zhong, J. Wang, J. M. Yan and X. B. Zhang, *Adv. Mater.*, 2016, **28**, 7948-7955.
18 J. C. Li, P. X. Hou, C. Shi, S. Y. Zhao, D. M. Tang, M. Cheng, C. Liu and H.-M. Cheng, *Carbon*, 2016, **109**, 632-639.
19 C. H. Choi, S. H. Park and S. I. Woo, *Appl. Catal. B*, 2012, **119–120**, 123-131.
20 R. Zhang, S. He, Y. Lu and W. Chen, *J. Mater. Chem. A*, 2015, **3**, 3559-3567.
21 M. Chen, P. Wu, L. Chen, S. Yang, L. Yu, Y. Ding, N. Zhu, Z. Shi and Z. Liu, *Sci. Rep.*, 2017, **7**, 4158.
22 A. Li, X. Mu, T. R. Li, H. Wen, W. Li, Y. Li and B. Wang, *Nanoscale*, 2018, DOI: 10.1039/C8NR02832J.
23 Y. Li, J. Kim, J. Wang, N.-l. Liu, Y. Bando, A. A. Alshehri, Y. Yamauchi, C.-H. Hou and K. C. W. Wu, *Nanoscale*, 2018, DOI: 10.1039/C8NR02288G.
24 Z. Wang, T. Yan, G. Chen, L. Shi and D. Zhang, *ACS Sustain. Chem. Eng.*, 2017, **5**, 11637-11644.
25 L. Li, S. Xiang, S. Cao, J. Zhang, G. Ouyang, L. Chen and C.-Y. Su, *Nat. Commun.*, 2013, **4**, 1774.
26 L. Cui, J. Wu and H. Ju, *ACS Appl. Mater. Interfaces*, 2014, **6**, 16210-16216.
27 E. S. Dragan, *Chem. Eng. J.*, 2014, **243**, 572-590.
28 L. H. Sperling, in *Interpenetrating Polymer Networks*, American Chemical Society, 1994, vol. 239, ch. 1, pp. 3-38
29 M. A. Haque, T. Kurokawa and J. P. Gong, *Polymer*, 2012, **53**, 1805-1822.
30 Y. Zhang, J. Liu, L. Huang, Z. Wang and L. Wang, *Sci. Rep*. 2015, **5**, 12374.
31 S. Saimani and A. Kumar, *J. Appl. Polym. Sci.*, 2008, **110**, 3606-3615.
32 S. Banerjee, G. Chaurasia, D. Pal, A. K. Ghosh, A. Ghosh and S. Kaity, *J. Sci. Ind. Res*., 2010, **69**, 777-784.
33 Q. Zhang, Z. Fang, Y. Cao, H. Du, H. Wu, R. Beuerman, M. B. Chan-Park, H. Duan and R. Xu, *ACS Macro Lett.*, 2012, **1**, 876-881.
34 P. E. Hande, S. Kamble, A. B. Samui and P. S. Kulkarni, *Ind. Eng. Chem. Res.*, 2016, **55**, 3668-3678.
35 A. Fathi, S. Lee, X. Zhong, N. Hon, P. Valtchev and F. Dehghani, *Polymer*, 2013, **54**, 5534-5542.
36 J. Zhao, X. Zhao, B. Guo and P. X. Ma, *Biomacromolecules*, 2014, **15**, 3246-3252.
37 C. Shen, Y. Li, H. Wang and Q. Meng, *RSC Adv.*, 2017, **7**, 18046-18053.
38 V. A. Blatov, L. Carlucci, G. Ciani and D. M. Proserpio, *CrystEngComm*, 2004, **6**, 377-395.
39 R. Vendamme, S. Y. Onoue, A. Nakao and T. Kunitake, *Nat. Mater.*, 2006, **5**, 494-501.
40 S. R. Batten, A. R. Harris, P. Jensen, K. S. Murray and A. Ziebell, *J. Chem. Soc., Dalton Trans.*, 2000, **0**, 3829-3836.
41 C. Zhang, S. Ding, J. Li, H. Xu, L. Sun, W. Wei, C. Li, J. Liu, X. Qu and Y. Lu, *Polymer*, 2008, **49**, 3098-3102.
42 T. M. Reineke, M. Eddaoudi, D. Moler, M. O'keeffe and O. Yaghi, *J. Am. Chem. Soc.*, 2000, **122**, 4843-4844.
43 M. Kondo, M. Shimamura, S. i. Noro, S. Minakoshi, A. Asami, K. Seki and S. Kitagawa, *Chem.Mater.*, 2000, **12**, 1288-1299.
44 E. H. Kim, Y. G. Jung and C. Y. Jo, *J. Nanomater.*, 2012, **2012**, 23.
45 L. Wang, Z. Gao, J. Chang, X. Liu, D. Wu, F. Xu, Y. Guo and K. Jiang, *ACS Appl. Mater. Interfaces*, 2015, **7**, 20234-20244.
46 D. Tiwari, C. Goel, H. Bhunia and P. K. Bajpai, *J. Environ. Manage.*, 2017, **197**, 415-427.

View Article Online
DOI: 10.1039/C8NJ03170C

47 K. Li, X. Xie and W.-D. Zhang, *ChemCatChem*, 2016, **8**, 2128-2135.
48 Y. Li, W. Zhou, H. Wang, L. Xie, Y. Liang, F. Wei, J. C. Idrobo, S. J. Pennycook and H. Dai, *Nat.Nanotechnol.*, 2012, **7**, 394-400.
49 M. Chen, P. Wu, L. Chen, S. Yang, L. Yu, Y. Ding, N. Zhu, Z. Shi and Z. Liu, *Sci. Rep.*, 2017, **7,** 4158.
50 E. Hu, X. Y. Yu, F. Chen, Y. Wu, Y. Hu and X. W. Lou, *Adv. Energy Mater.*, 2018, **8**, 1702476.
51 X. Li, Y. Fang, S. Zhao, J. Wu, F. Li, M. Tian, X. Long, J. Jin and J. Ma, *J. Mater. Chem. A*, 2016, **4**, 13133-13141.
52 G. Ren, X. Lu, Y. Li, Y. Zhu, L. Dai and L. Jiang, *ACS Appl. Mater. Interfaces*, 2016, **8**, 4118-4125.
53 T. Zhou, Y. Zhou, R. Ma, Q. Liu, Y. Zhu and J. Wang, *J. Mater. Chem. A*, 2017, **5**, 12243-12251
54 X. Qiao, J. Jin, H. Fan, Y. Li and S. Liao, *J. Mater. Chem. A*, 2017, **5**, 12354-12360.
55 N. K. Chaudhari, M. Y. Song and J. S. Yu, *Sci. Rep.*, 2014, **4,** 5221.
56 V. Kashyap, S. K. Singh and S. Kurungot, *ACS Appl. Mater. Interfaces*, 2016, **8**, 20730-20740.
57 B. Wang, L. Xu, G. Liu, P. Zhang, W. Zhu, J. Xia and H. Li, *J. Mater. Chem. A*, 2017, **5**, 20170.
58 Y. Ni, L. Yao, Y. Wang, B. Liu, M. Cao and C. Hu, *Nanoscale*, 2017, **9**, 11596-11604.
59 J. Zhu, H. Zhou, C. Zhang, J. Zhang and S. Mu, *Nanoscale*, 2017, **9**, 13257-13263.
60 M. Thomas, R. Illathvalappil, S. Kurungot, B. N. Nair, A. P. Mohamed, G. M. Anilkumar, T. Yamaguchi and U. S. Hareesh, *ACS Appl. Mater. Interfaces*, 2016, **8** (43), 29373-29382.
61 T. D. Thanh, N. D. Chuong, J. Balamurugan, H. Van Hien, N. H. Kim and J. H. Lee, *Small*, 2017, **13**, 1701884.
62 R. Illathvalappil, V. M. Dhavale, S. N. Bhange and S. Kurungot, *Nanoscale*, 2017, **9**, 9009-9017.
63 W. J. Jiang, L. Gu, L. Li, Y. Zhang, X. Zhang, L. J. Zhang, J. Q. Wang, J. S. Hu, Z. Wei and L. J. Wan, *J. Am. Chem. Soc.*, 2016, **138**, 3570-3578.
64 C. Zhang, J. Liu, Y. Ye, Z. Aslam, R. Brydson and C. Liang, *ACS appl. Mater. Interfaces*, 2018, **10**, 2423.
65 C. Zhu, S. Fu, J. Song, Q. Shi, D. Su, M. H. Engelhard, X. Li, D. Xiao, D. Li and L. Estevez, *small*, 2017, **13**, 1603407.
66 O. L. Li, S. Chiba, Y. Wada, G. Panomsuwan and T. Ishizaki,*J. Mater.Chem. A*, 2017, **5**, 2073-2082.
67 X. F. Li, K. Y. Lian, L. Liu, Y. Wu, Q. Qiu, J. Jiang, M. Deng and Y. Luo, *Sci. Rep*., 2016, **6**, 23495.
68 X. Huang, Z. Yang, B. Dong, Y. Wang, T. Tang and Y. Hou, *Nanoscale*, 2017, **9**, 8102-8106.
69 L. Zhou, C. Yang, J. Wen, P. Fu, Y. Zhang, J. Sun, H. Wang and Y. Yuan, *J. Mater. Chem. A*, 2017, **5**, 19343-19350.
70 K. Shijina, R. Illathvalappil, S. Kurungot, B. N. Nair, A. P. Mohamed, T. Yamaguchi, G. M. Anilkumar, U. S. Hareesh and G. S. Sailaja, *ChemistrySelect*, 2017, **2** (28), 8762-8770**.**

View Article Online
DOI: 10.1039/C8NJ03170C

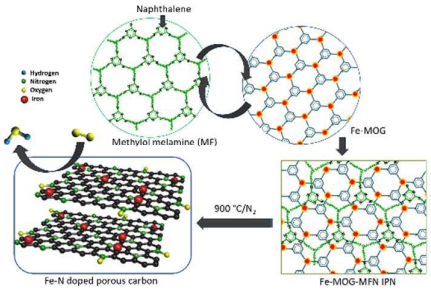

High surface area heteroporous Fe-N doped carbon derived from metal organic gel- melamine formaldehyde interpenetrating networks as a durable oxygen reduction reaction catalyst.